ATHEROSCLEROSIS

Atherosclerotic disease activity is associated with glycolytic enzyme expression across multiple cell types and is trackable by FDG-PET

Paula Nogales[1,2]*, Carlos Velasco[1], Leticia González-Cintado[1], Diana Sharysh[2], Adriana Mota-Cobián[3], Raúl Izquierdo-Serrano[1], Carlos Torroja[1], David del Rio-Aledo[1], Daniel Morales-Cano[1], Rubén A. Mota[4], Alberto Benguría[1], Ana Dopazo[1,5], Fátima Sánchez-Cabo[1], Jesús Vázquez[1,5], Samuel España[1,3,6], Laura Carramolino[1], Jesús Mateo[1], Jacob F. Bentzon[1,2,7]*

Positron emission tomography (PET) imaging with the radiolabeled glucose analog fluorodeoxyglucose (^{18}FDG) is used to monitor atherosclerosis in clinical trials, but there is uncertainty regarding the plaque cell types that accumulate FDG and how uptake is regulated. The long-standing view that ^{18}FDG is mainly taken up by macrophages is at odds with human and experimental data, and the impact of disease activity on ^{18}FDG uptake has not been examined directly. To analyze the ability of ^{18}FDG-PET to monitor disease activity, we developed a model of plaque regression in minipigs with hepatic overexpression of a gain-of-function mutant of *proprotein convertase subtilisin/kexin type 9* (*PCSK9*). Atherosclerosis was induced through 12 months of high-fat feeding in the porcine model. Disease activity was then lowered for 3 months by reducing plasma cholesterol with a low-fat diet alone or in combination with the microsomal transfer protein (MTP) inhibitor BMS-212122. Plaque regression in advanced lesions of the abdominal aorta was evident from reduced lipid content, reduced necrotic core size, and partial resolution of plaque inflammation and was accompanied by a decline in ^{18}FDG-PET signal. Single-cell gene expression profiling revealed that plaque regression involved substantial down-regulation of genes encoding glycolytic enzymes in smooth muscle cells (SMCs), macrophages, and lymphocytes, which was corroborated by analysis of the plaque cellular proteome. These findings in a large-animal model suggest that ^{18}FDG-PET can monitor atherosclerosis because of a close association between disease activity and glycolytic enzyme expression in all of the major plaque cell types.

INTRODUCTION

Noninvasive arterial imaging plays an increasingly important role in the clinical management of atherosclerosis. Measurement of atherosclerotic plaque burden by coronary computed tomography (CT) angiography or carotid three-dimensional ultrasound can diagnose the disease and provide a more accurate risk stratification than conventional risk factor scoring alone (*1*). However, even with effective therapy, changes in plaque burden are slow (*2*–*4*), and there is a need for imaging tools that can monitor changes in disease activity (the rate of plaque progression or regression). Such modalities would allow the assessment of treatment efficacy, prediction of disease progression, and tailoring of therapies for personalized medicine.

The most suitable available imaging modality for detecting molecular changes in atherosclerosis is positron emission tomography (PET), and PET imaging with the radiotracer ^{18}F-fluorodeoxyglucose (^{18}FDG) has been used extensively to monitor treatment responses, analyze risk-factor associations, and predict future event risk in patients with atherosclerosis (*5*, *6*). The ability of ^{18}FDG-PET to measure disease activity is supported by the reduction in ^{18}FDG-PET signal in patients treated with therapies that lower apolipoprotein B–containing lipoproteins (APOB-LPs), such as statins, lipoprotein apheresis, and proprotein convertase subtilisin/kexin type 9 (PCSK9) inhibitors (*7*–*9*), which are interventions that are known to reduce plaque progression (*4*).

^{18}FDG is taken up by cells through the glucose transport machinery but cannot be metabolized, allowing its accumulation to serve as a readout of glucose uptake. Initial studies examining ex vivo ^{18}FDG plaque uptake and correlations between ^{18}FDG-PET signal and macrophage content in endarterectomies suggested that FDG is primarily taken up by plaque macrophages (*10*, *11*), positing ^{18}FDG-PET imaging as a direct measure of plaque inflammation. However, it is not clear why glucose uptake should be selective for macrophages in atherosclerosis, and other studies have indicated that ^{18}FDG uptake occurs in multiple cell types in the plaque (*5*, *12*). In a previous study, we mapped FDG uptake in atherosclerotic lesions of minipigs and found similar uptake in macrophage-rich and macrophage-poor plaque regions, indicating uptake by nonmacrophage cell types, including smooth muscle cells (SMCs) (*12*). Although these findings indicate that ^{18}FDG-PET does not specifically image arterial macrophages, they leave unanswered the question of how ^{18}FDG PET tracks atherosclerotic disease activity.

To address this question, here, we developed a human-sized–animal model in which atherosclerotic plaques can be induced and subsequently regressed at the time of choice. The model uses minipigs with hepatic overexpression of a gain-of-function mutant of *PCSK9* (*PCSK9*^{D374Y}), which results in efficient down-regulation of hepatic low-density lipoprotein receptors, high circulating APOB-LP concentrations on a high-fat diet, and the development of atherosclerotic lesions with human-like morphological features (*13*).

[1]Centro Nacional de Investigaciones Cardiovasculares Carlos III (CNIC), Madrid 28029, Spain. [2]Department of Clinical Medicine, Aarhus University, Aarhus 8200, Denmark. [3]Universidad Complutense de Madrid, Madrid 28040, Spain. [4]Universidad Europea de Madrid SLU, Villaviciosa de Odón 28670, Spain. [5]CIBER de Enfermedades Cardiovasculares (CIBERCV), Madrid 28029, Spain. [6]Instituto de Tecnologías Físicas y de la Información Leonardo Torres Quevedo, Consejo Superior de Investigaciones Científicas, Madrid 28006, Spain. [7]Steno Diabetes Center Aarhus and Department of Cardiology, Aarhus University Hospital, Aarhus 8200, Denmark.
*Corresponding author. Email: pnogales@cnic.es (P.N.); jfbentzon@cnic.es (J.F.B.)

By lowering APOB-LPs to reduce disease activity and analyzing the effects on arterial ^{18}FDG-PET signal alongside plaque cell states, we aimed to clarify the mechanisms linking disease activity to ^{18}FDG uptake in atherosclerotic arteries.

RESULTS

Atherosclerosis regression model in *PCSK9*^{D374Y} minipigs

PCSK9^{D374Y} transgenic Yucatan minipigs ($n = 23$, males, 3 months old) were randomized into three groups (Fig. 1A). All groups were fed a high-fat, high-cholesterol (HFHC) diet for 1 year to induce atherosclerosis. One group was euthanized without further intervention (baseline group, $n = 7$). Pigs in the other groups were switched to a low-fat (LF) diet for a further 3 months either with no additional treatment to achieve moderate APOB-LP lowering (LF group, $n = 8$) or with daily supplementation with the microsomal transfer protein (MTP) inhibitor (MTPi) BMS-212122 (loading dose 1 mg/kg per day in week 1, maintenance dose of 0.5 mg/kg per day) to achieve stronger APOB-LP lowering (LF/MTPi group, $n = 8$). MTP inhibition reduces plasma APOB-LP by blocking the transfer of lipids to nascent APOB in the liver and intestine and has a narrow clinical indication to treat patients with homozygous familial hyper-

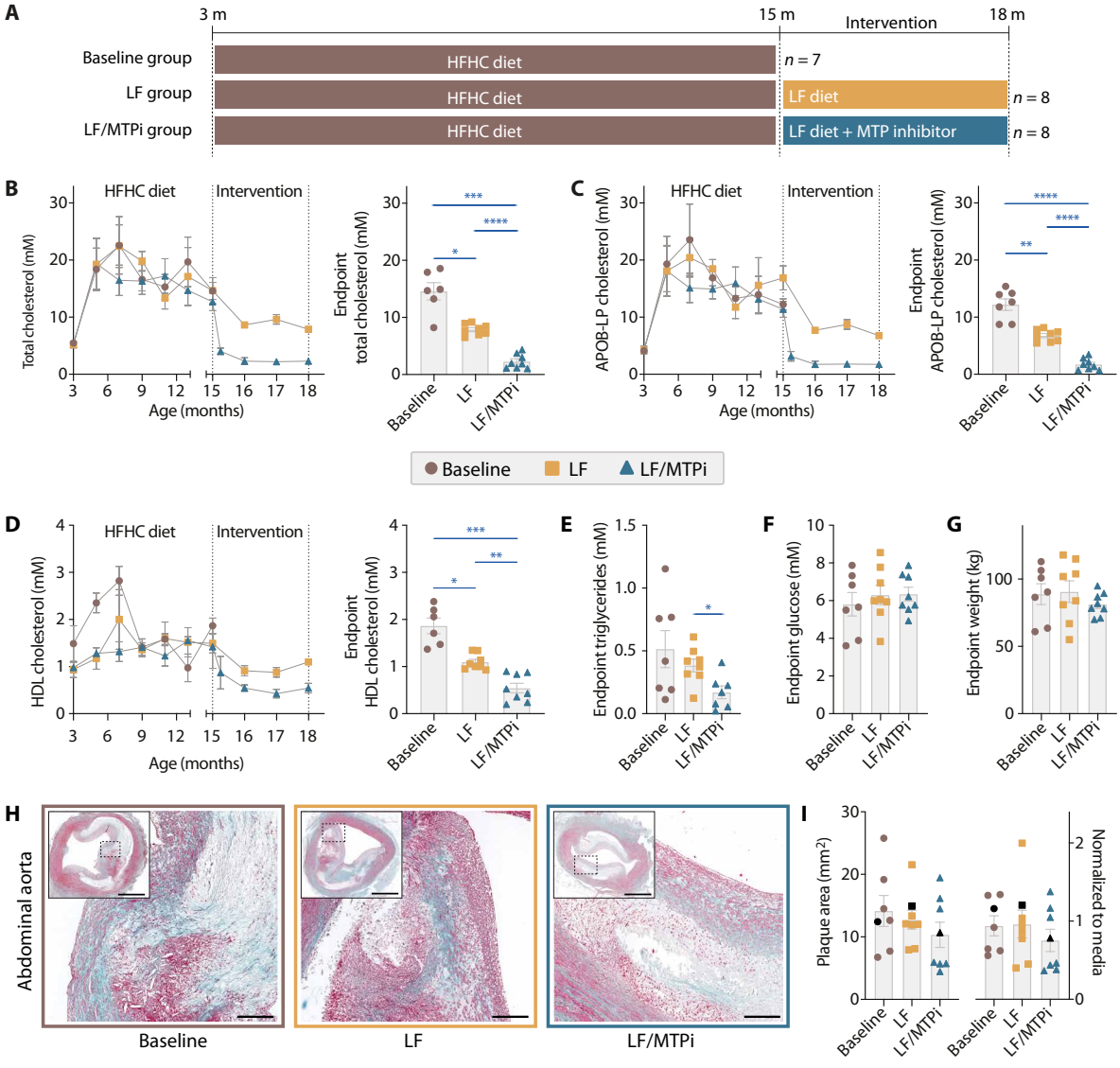

Fig. 1. LF diet and MTP inhibition reduce APOB-LP cholesterol to clinical target values. (**A**) The study design timeline is shown. (**B**) Evolution of plasma total cholesterol is shown over time (left). End-point total cholesterol is shown for each group (right). (**C**) Plasma APOB-LP cholesterol is shown over time (left). End-point APOB-LP cholesterol is shown for each group (right). (**D**) Plasma HDL cholesterol is shown over time (left). End-point HDL cholesterol is shown for each group (right). (**E**) End-point plasma triglycerides are shown for each group. (**F**) End-point plasma glucose and (**G**) body weight are shown for all groups. (**H**) Representative Masson's trichrome–stained sections of abdominal aorta lesions show fibroatheromas with lipid pools and early necrotic core formation. Scale bars, 2.5 mm in overview insets and 0.5 mm in the magnified views of the dotted area. (**I**) Plaque area (left) and normalized plaque area (to adjacent media area) (right). Points represent the average area in serial sections along the abdominal aorta; black points mark the pigs from which image examples are shown. Bars in (B) to (G) and (I) show means ± SEM. Statistical analyses for differences between baseline ($n = 7$), LF ($n = 8$), and LF/MTPi pigs ($n = 8$) in (B) to (G) and (I) were performed using Brown-Forsythe and Welch ANOVA with Dunnett's T3 posttest. *$P < 0.05$; **$P < 0.01$; ***$P < 0.001$; ****$P < 0.0001$.

cholesterolemia (*14*). The effective dose was determined in pilot studies (fig. S1).

MTP inhibition achieves clinical-target APOB-LP lowering

All experimental groups developed severe and similar amounts of hypercholesterolemia on the HFHC diet during the 12-month atherosclerosis induction period (Fig. 1, B and C). At the end point, APOB-LP cholesterol in the baseline group was 12.2 ± 2.6 mM (means ± SEM). Three months on the LF diet substantially decreased APOB-LP cholesterol (to 6.8 ± 1.0 mM at the end point), but it remained in the range considered atherogenic in humans (*15*). In the LF/MTPi group, the addition of MTP inhibition resulted in additional further reduction (to 1.8 ± 1.0 mM at the end point) in comparison with that in the LF diet group. High-density lipoprotein (HDL) cholesterol was also decreased in LF and LF/MTPi pigs compared with that in baseline pigs, most likely as a secondary effect of the reduction in APOB-LP (Fig. 1D). Triglycerides were reduced only in the LF/MTPi group (Fig. 1E), whereas plasma glucose and body weight remained unchanged in both intervention groups (Fig. 1, F and G). No signs of MTPi-induced liver toxicity were detected (fig. S2, A and B).

Plaque size is not altered by APOB-LP lowering for 3 months

Atherosclerotic plaques were examined in serial sections from the abdominal aorta (measured from the most distal renal artery branch point to the aortic trifurcation), the common iliac arteries, and the proximal left anterior descending artery (LAD) and in a single section from the bifurcation of the LAD and the circumflex (CX) artery (LAD/CX bifurcation). Atherosclerosis was most advanced in the abdominal aorta, and fibroatheromas or extensive pathological intimal thickenings were found in all pigs. Other vessels contained intimal xanthomas, small pathological intimal thickenings, and some fibroatheromas. Lesions at the LAD/CX bifurcation differed from the rest by consisting almost exclusively of foam-cell accumulations. Examples of plaque morphology in the abdominal aorta and other sites are shown in Fig. 1H and fig. S3. Overall plaque size was not changed by 3 months of APOB-LP lowering in any of the arterial beds, whether measured as the absolute intima area or after normalization to arterial media area (Fig. 1I and fig. S3, A to C).

APOB-LP lowering reduces plaque lipid content and the size of the necrotic core

Analysis of the major structural plaque components revealed a lower content of oil red O–stained neutral lipids in LF/MTPi pigs at all examined vascular sites (Fig. 2, A and B; and fig. S4, A and B). In LF pigs, lipid depletion was detected in the less-advanced lesions of the coronary and iliac arteries (fig. S4, A and B) but not in abdominal aorta plaques (Fig. 2B). The necrotic core size was substantially reduced in abdominal aorta plaques of LF/MTPi pigs, whereas the effect of LF diet alone was modest and statistically insignificant (Fig. 2, C and D). Necrotic core size could not be measured at other sites because of the early stage of atherosclerosis. Sirius red staining of collagen-rich tissue revealed no change in absolute area after APOB-LP lowering in any vascular bed (Fig. 2, E and F, and fig. S5A). However, the relative content of collagen-rich tissue was higher in abdominal aorta plaques of LF/MTPi pigs compared with the other two experimental groups, at least partly explained by the shrinking necrotic core (Fig. 2, E and F). A similar pattern was observed for plaque cellularity; no changes were found in total plaque cells in any vascular bed, but an increase in average cell density, without more cell proliferation, was noted in abdominal plaques of LF/MTPi pigs (figs. S5B and S6). The experimental groups showed no differences in plaque calcification (detected by staining with alizarin red) at any site (Fig. 2, G and H, and fig. S5C).

Fibrous cap thickness is unchanged and mature neovessels increased after APOB-LP lowering

The fibrous cap is a layered subendothelial assembly of SMCs that prevents plaques with a necrotic core (fibroatheromas) from rupturing, causing thrombosis, and precipitating a heart attack or ischemic stroke (*16*). Intravascular imaging by optical coherence tomography in patients has indicated that the fibrous cap may thicken after APOB-LP lowering (*17*); however, the impact of APOB-LP lowering on cap thickness and SMC content has not previously been analyzed directly by microscopy in plaques with human-like features. SMCs were counted by staining for ACTA2 (actin, alpha 2, smooth muscle, aorta). As expected, most $ACTA2^+$ cells were located in the subendothelial cap structure, but there were no differences in ACTA2-stained areas between groups in any of the arterial beds studied (Fig. 3, A and B, and fig. S5D). Likewise, the minimum thickness of the fibrous cap in abdominal aorta fibroatheromas showed no variation between the experimental groups; however, an upward trend in cap thickness was observed in the LF/MTPi group (Fig. 3C).

Atherosclerotic lesions in humans and pigs, but not the small lesions in mice, are nourished by intraplaque neovessels (*18*). To examine their behavior during plaque regression, we counted the number of vessel profiles in sections of abdominal aorta stained for CD31 and ACTA2 and found an increase in the number of mature SMC-enveloped intraplaque vessels after 3 months of APOB-LP–lowering treatment (Fig. 4, A to C).

APOB-LP lowering triggers regional depletion of macrophages in plaques

Plaque inflammation rapidly resolves upon APOB-LP lowering in mouse models of atherosclerosis, leading to almost complete loss of plaque macrophages within a few months (*19*, *20*). To investigate changes in plaque macrophage content in the pig regression model, we stained for the pan-macrophage markers CD68 and LYZ (lysozyme). Macrophage content was nominally lower in the LF/MTPi group than in the LF and baseline groups in the abdominal aorta (Fig. 5, A to D) and other examined arterial beds (fig. S5E); however, the differences were only statistically significant ($P = 0.034$) at the LAD/CX bifurcation (fig. S5E). The more pronounced reduction in macrophages at this site can be attributed to these lesions being almost exclusively composed of foam cells, as noted above.

The shoulder region of fibroatheromas is a particularly active and the most common site of plaque rupture (*21*). Separate analysis of $CD68^+$ and LYZ^+ areas in the shoulder regions of eccentric abdominal aorta lesions revealed significant reductions in the LF/MTPi group ($P = 0.048$ for $CD68^+$ and $P = 0.043$ for LYZ^+ areas), suggesting that APOB-LP lowering resolves inflammation in the shoulder region first (Fig. 5, E and F). A similar trend was observed for eccentric iliac plaques (fig. S7), whereas lesions at other sites were not sufficiently advanced for this type of analysis.

^{18}FDG-PET detects the reduction in disease activity after APOB-LP lowering

^{18}FDG-PET/CT imaging of the abdominal aorta was performed in all pigs at the end of the study and in a concurrent group of age-matched

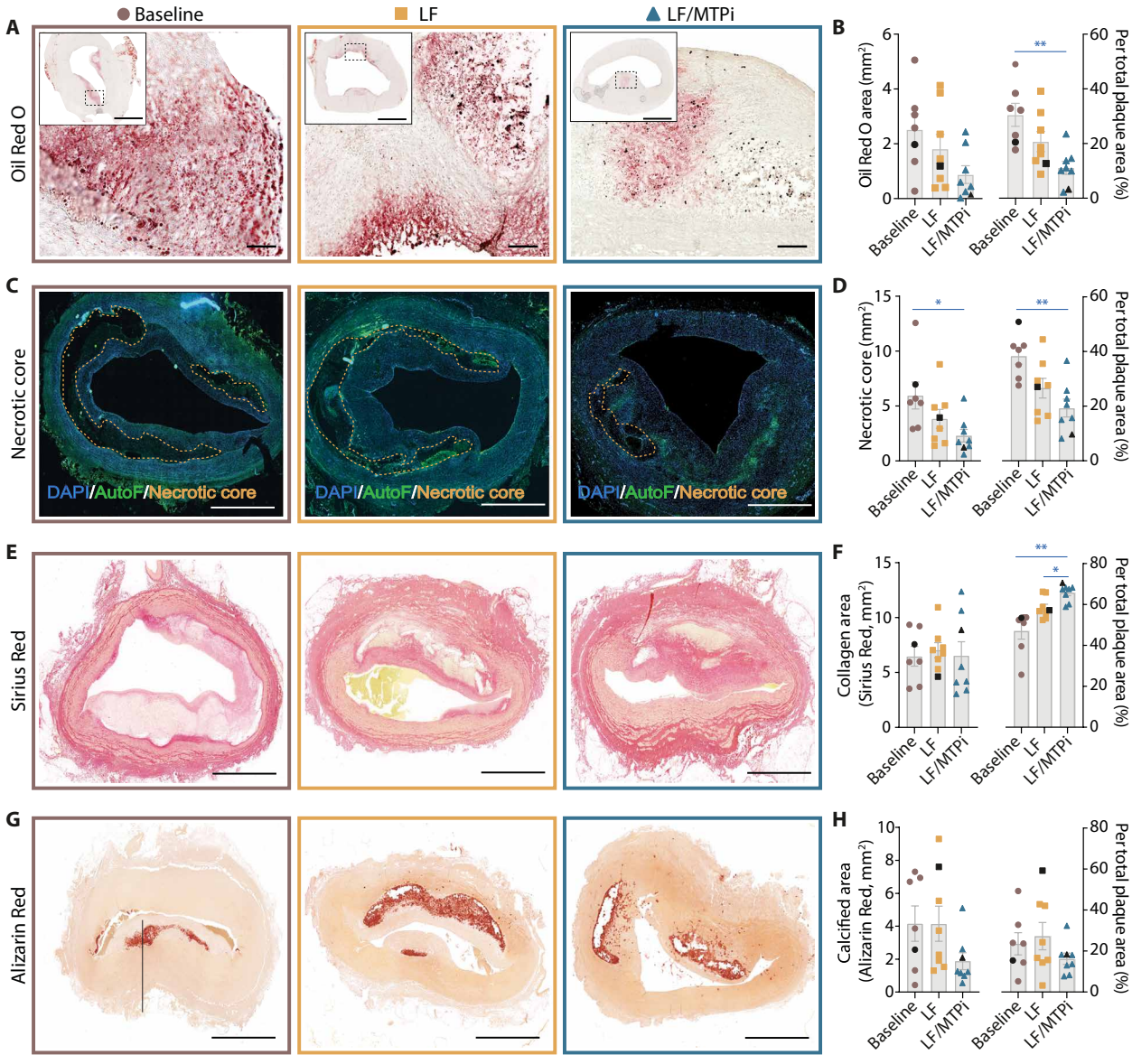

Fig. 2. APOB-LP lowering decreases plaque lipids and necrotic core. (**A**) Representative images and (**B**) quantification of oil red O staining in abdominal aorta plaques from the baseline, LF, and LF/MTPi groups, including absolute values (left) and normalized to plaque area (right). Scale bars, 2.5 mm in overview insets and 0.5 mm in magnified views of the dotted areas. (**C**) Necrotic core area is shown in fluorescence images, measured as acellular regions in DAPI-stained sections. DAPI is shown in blue, autofluorescence in green, and necrotic core is demarked by orange dashed lines. Scale bars, 2.5 mm. (**D**) Quantification of necrotic core area, including absolute values (left) and normalized to plaque area (right). (**E**) Representative images and (**F**) quantification of Sirius red staining of collagen-rich plaque tissue are shown for all groups, including absolute values (left) and normalized to plaque area (right). Scale bars, 2.5 mm. (**G**) Alizarin red–stained calcified plaque tissue images and (**H**) quantification are shown for all groups, including absolute values (left) and normalized to plaque area (right). Scale bars, 2.5 mm. Points represent the average of serial sections along the abdominal aorta, except in (B), where a single cryosectioned segment per pig was analyzed. Bars in (B), (D), (F), and (H) show means ± SEM. Statistical analyses for differences between baseline ($n = 7$), LF ($n = 8$), and LF/MTPi pigs ($n = 8$) were performed using ANOVA with Tukey's posttest in (B) and (D), Brown-Forsythe and Welch ANOVA with Dunnett's T3 posttest in (F), and Kruskal-Wallis test in (H). *$P < 0.05$; **$P < 0.01$.

nonatherosclerotic wild-type (healthy) minipigs ($n = 5$) maintained on the LF diet. The abdominal aorta was selected for these studies because of its advanced state of atherosclerosis and because the coronary and iliac arteries are influenced by spillover signals from the myocardium and bladder. The carotid bifurcation, a typical site for imaging in humans, is anatomically different in pigs.

The ^{18}FDG-PET signal was quantified as the mean and maximum standardized uptake values (SUVs) in 32 ± 8-mm-long segments along the abdominal aorta and then averaged to provide single readouts for each pig (Fig. 6A). The mean SUV_{mean} was lower in the LF/MTPi group than in the baseline group (1.04 ± 0.28 versus 1.54 ± 0.24), and the mean SUV_{max} in LF/MTPi pigs was lower than those in both the baseline and the LF groups (1.21 ± 0.28 versus 1.84 ± 0.39 and 1.68 ± 0.36, respectively) (Fig. 6B). The 3 months of ApoB-LP lowering in the LF/MTPi group reverted both ^{18}FDG-PET metrics to the values observed in the nonatherosclerotic pigs. The background

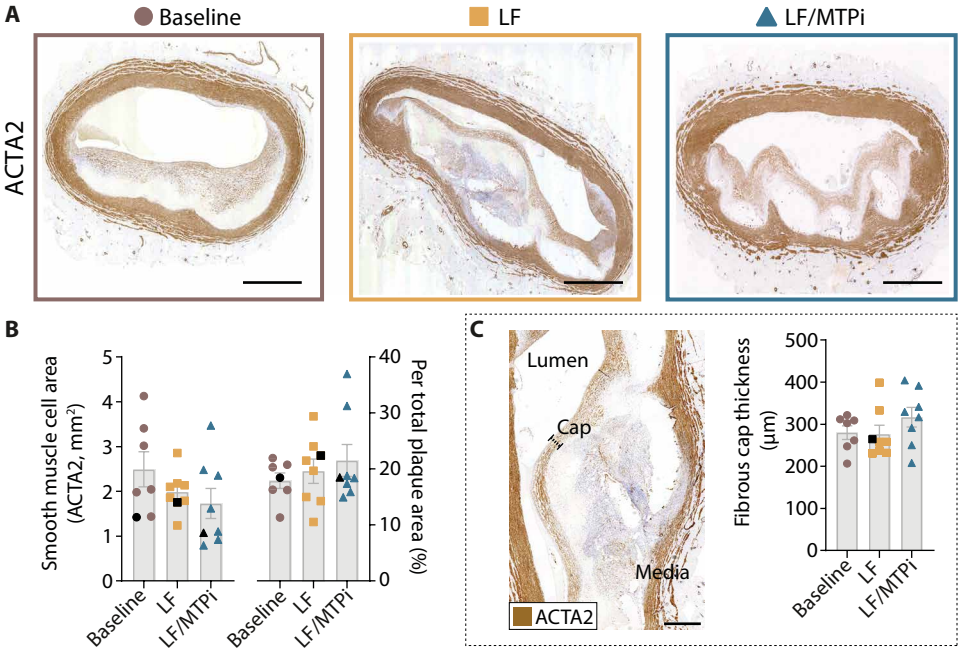

Fig. 3. APOB-LP lowering does not alter plaque SMC content or fibrous cap thickness. (**A**) Representative images and (**B**) quantification of the plaque area occupied by ACTA2$^+$ contractile SMCs, including absolute values (left) and normalized to plaque area (right). Scale bars, 2.5 mm. (**C**) A representative image of fibrous cap (left). Scale bar, 0.5 mm. Fibrous cap thickness (right), measured as the minimal distance between the lumen and necrotic core, as indicated by the dotted bar in the representative image. Points in (B) and (C) represent the average area in serial sections along the abdominal aorta for each pig, and bars show means ± SEM; black points mark the pigs from which image examples are shown. Statistical analysis for differences between baseline ($n = 7$), LF ($n = 8$), and LF/MTPi pigs ($n = 8$) in (B) and (C) was performed using the Kruskal-Wallis test.

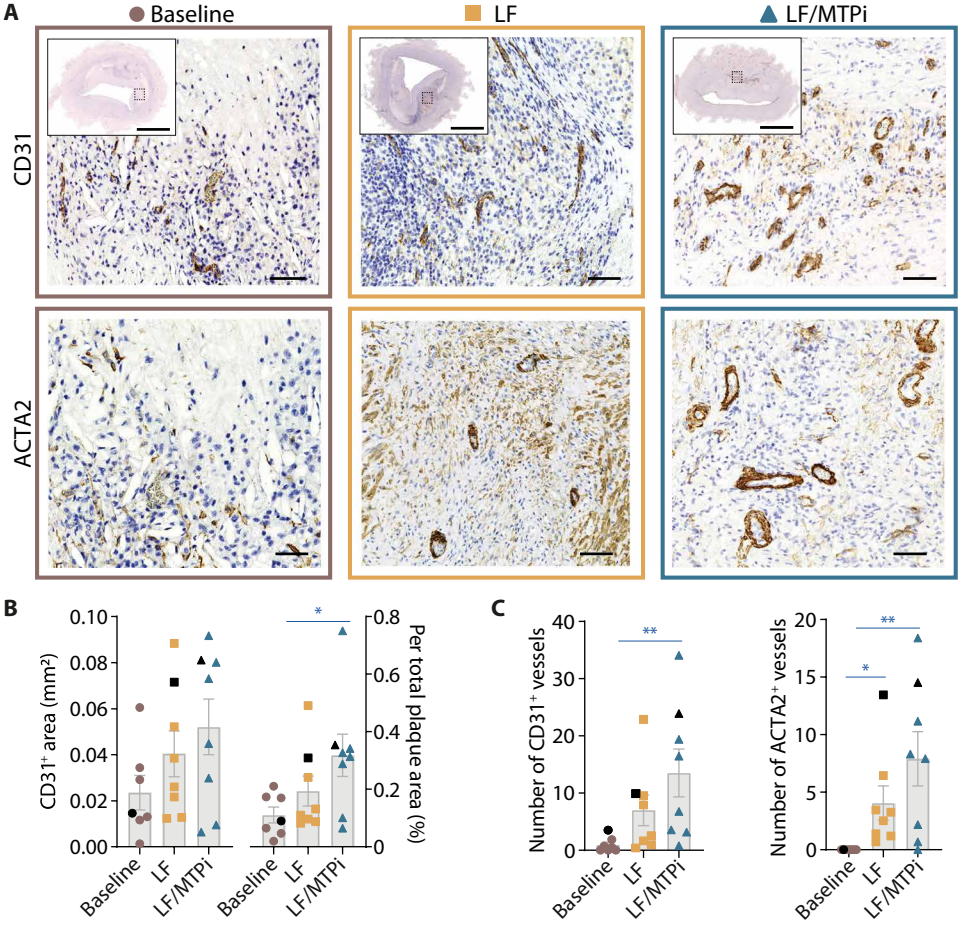

Fig. 4. APOB-LP lowering increases mature intraplaque vessels. (**A**) Representative images of CD31 (top) and ACTA2 (bottom) immunostaining in consecutive sections of abdominal aorta plaques from the baseline, LF, and LF/MTPi conditions. Scale bars, 2.5 mm in overview insets and 0.25 mm in magnified views of the dotted areas. (**B**) CD31$^+$ absolute area (left) and normalized to plaque area (right) analyses are shown for all conditions. (**C**) Quantification of CD31$^+$ (left) and ACTA2$^+$ (right) neovessels is shown for all conditions. Points in (B) and (C) represent the average values in serial sections along the abdominal aorta for each pig, and bars show means ± SEM; black points mark the pigs from which image examples are shown. Statistical analysis for differences between baseline ($n = 7$), LF ($n = 8$), and LF/MTPi pigs ($n = 8$) in (B) and (C) was performed using Kruskal-Wallis test with Dunn's posttest. *$P < 0.05$; **$P < 0.01$.

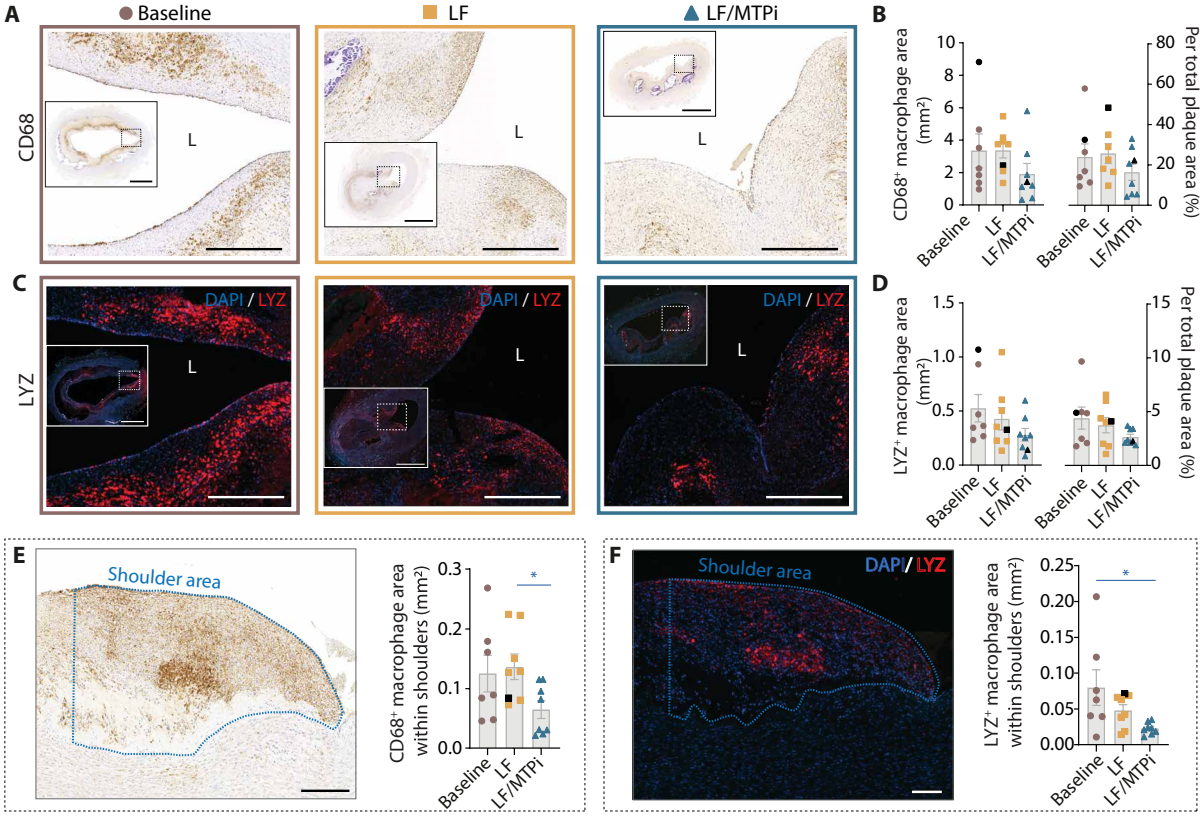

Fig. 5. APOB-LP lowering reduces macrophage content in the plaque shoulder region. (**A**) Representative CD68 immunostaining in sections of abdominal aorta plaques are shown. Scale bars, 2.5 mm in overview insets and 0.5 mm in magnified views of the dotted areas. (**B**) The bar plots show mean absolute (left) and relative (right) stained areas for total CD68$^+$ macrophage plaque content for all conditions. (**C**) Representative LYZ immunostaining (red, DAPI shown in blue) in sections of abdominal aorta plaques is shown. Scale bars, 2.5 mm in overview insets and 0.5 mm in magnified views of the dotted areas. (**D**) The bar plots show mean absolute (left) and relative (right) stained areas for total LYZ$^+$ macrophage plaque content for all conditions. (**E**) Representative image (left) of CD68 immunostaining in the shoulder region (demarcated with a blue dotted line) in abdominal aorta plaques. Scale bar, 0.5 mm. The bar plot (right) shows the macrophage marker–stained area in shoulder regions for all conditions. (**F**) Representative image (left) of LYZ immunostaining (red, DAPI shown in blue) in the shoulder region (demarcated with a blue dotted line) in abdominal aorta plaques. Scale bar, 0.5 mm. The bar plot (right) shows the macrophage marker–stained area in shoulder regions. Points in (B) and (D) to (F) represent the average area in serial sections along the abdominal aorta for each pig, and bars show means ± SEM; black points mark the pigs from which image examples are shown. Statistical analyses for differences between baseline ($n = 7$), LF ($n = 8$), and LF/MTPi pigs ($n = 8$) were performed using one-way ANOVA in (B), Kruskal-Wallis test with Dunn's posttest in (D) and (E), and Brown-Forsythe and Welch ANOVA with Dunnett's T3 posttest in (F). *$P < 0.05$.

^{18}FDG signal in the abdominal vena cava was similar in all groups (Fig. 6B). Analysis of calcium scores in the CT images showed no differences in calcified plaque burden among the atherosclerotic pigs (Fig. 6C), consistent with the histological analysis.

^{18}FDG-PET changes induced by APOB-LP lowering are not explained by alterations in plaque cellular composition

To determine whether modifications in macrophage content or other plaque attributes could explain the reduction in the ^{18}FDG-PET signal in regressing plaques, we performed a linear regression analysis comparing SUV_{mean} values with plaque size, nonnecrotic plaque area, LYZ$^+$ and CD68$^+$ macrophages, ACTA2$^+$ SMCs, total plaque nuclei, and neovessels (fig. S8). Correlations were significant for plaque size [$P = 0.02$, coefficient of determination (R^2) = 0.25] and ACTA2$^+$ SMCs ($P = 0.005$, $R^2 = 0.33$), borderline significant for LYZ$^+$ macrophages ($P = 0.05$, $R^2 = 0.18$), and not significant for the other examined plaque features (fig. S8). None of these features thus explained the observed change in FDG-PET/CT signal, because they were either not strongly related to FDG-PET/CT signal, as in the case of macrophages or neovessels, or not altered during plaque regression, as in the case of plaque size or SMCs.

Glycolytic enzyme expression is reduced in multiple cell types in regressing plaques

As an alternative explanation, we hypothesized that the ^{18}FDG-PET signal alteration might be the result of changes in glucose consumption in one or more plaque cell types. Directly detecting glucose uptake by microautoradiography has limited resolution. Therefore, we instead used single-cell RNA sequencing (scRNA-seq) to produce single-cell gene expression signatures of progressing and regressing atherosclerotic plaques in *PCSK9*^{D374Y} minipigs. We reasoned that these data would reveal glycolytic activity, given that long-term glycolytic flux is regulated transcriptionally (*22*–*24*).

To produce these signatures, we randomized *PCSK9*^{D374Y} pigs (males and females) into two experimental groups: an actively progressing atherosclerosis group maintained for 15 months on the HFHC diet (HFHC group: females, $n = 5$; males, $n = 2$) and an LF/MTPi group fed for 12 months on the HFHC diet and then switched to the LF

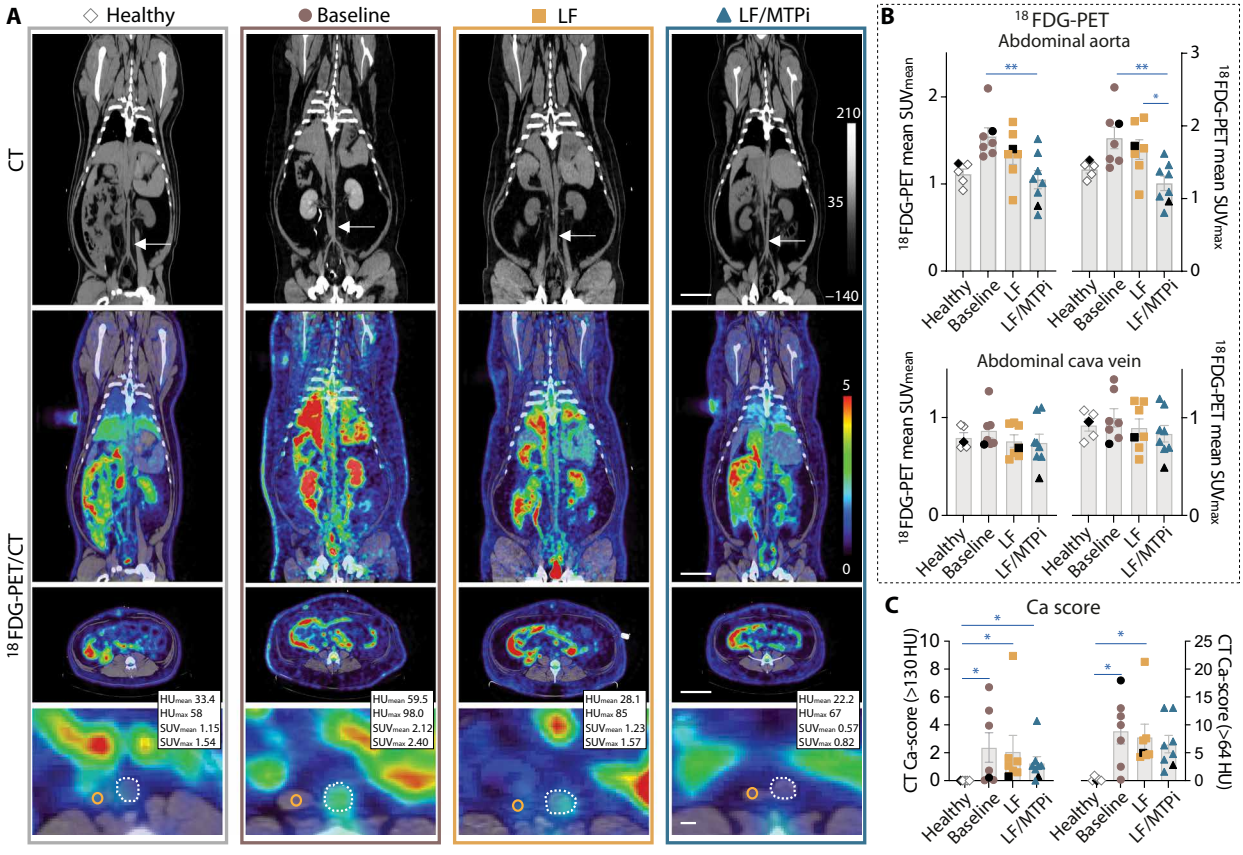

Fig. 6. ^{18}FDG-PET detects reduced disease activity. (**A**) Representative CT and ^{18}FDG-PET/CT images in the coronal and transverse planes (arrow position in the CT image) from baseline, LF, LF/MTPi, and age-matched healthy pigs. The bottom row shows higher magnification views of the transverse plane with regions marked for quantification around the aorta (white dotted circles) and in the inferior vena cava (orange circles). Signal values are shown for the aorta region of interest. Scale bars, 50 mm in overviews and 10 mm in magnified areas. Scales for CT images, representing Hounsfield units (HU), and for PET images, representing SUVs, apply to all images. (**B**) Mean SUV_{mean} (top left) and SUV_{max} (top right) in the abdominal aorta (top plots). The same is shown for the abdominal cava vein in the bottom plots. (**C**) Conventional (greater than 130 HU) and lowered-threshold (>64 HU) calcium (Ca) scores. Points in (B) and (C) represent the average along the abdominal aorta for each pig, and bars show means ± SEM; black points mark the pigs from which image examples are shown. Statistical analysis for differences between healthy ($n = 5$), baseline ($n = 7$), LF ($n = 7$), and LF/MTPi pigs ($n = 8$) in (B) and (C) was performed using one-way ANOVA and Tukey's posttest. $^{*}P < 0.05$; $^{**}P < 0.01$.

diet plus MTP inhibition for 3 months (females, $n = 4$; males, $n = 1$) (Fig. 7A). At the end of the experiment, plaque tissue was dissected from the distal abdominal aorta and rapidly processed for scRNA-seq.

Nonlinear dimensionality reduction and clustering of the scRNA-seq data separated plaque cells into four superclusters, identified by canonical marker expression (fig. S9): T lymphocytes; macrophages, monocytes, and dendritic cells (DCs); SMCs and their modulated progeny; and endothelial cells (Fig. 7B). Within these clusters, we performed a differential gene expression analysis of glycolytic pathway genes. All major cell types in regressing plaques showed reduced expression of the entire glycolytic chain from hexokinase to lactate dehydrogenase (Fig. 7, C and D). These changes were more pronounced in the SMC supercluster, followed by the lymphocyte and macrophage superclusters, and were less pronounced in the small endothelial cell supercluster. No broad changes in the expression of genes in other metabolic pathways were detected (figs. S10 and S11). *MTP* expression was not detected in plaque cells.

To confirm that glycolytic gene expression changes occurred in the specific *PCSK9*^{D374Y} minipigs used in the ^{18}FDG-PET imaging experiment, we conducted a quantitative polymerase chain reaction (PCR) analysis of the expression of critical glycolytic genes in sections of abdominal aorta plaques from those animals. Almost all of the selected genes showed a down-regulation after 3 months of ApoB-LP lowering in LF/MTPi pigs versus the baseline and LF groups (Fig. 7E).

Last, we validated the findings on the protein level through proteomics of residual plaque cell suspensions from the scRNA-seq experiment, confirming the down-regulation of the class of glycolytic proteins in the LF/MTPi group (Fig. 7, F and G). The combined results thus suggest that ^{18}FDG-PET imaging provides a valid readout of disease activity in atherosclerosis, not because it tracks plaque macrophages, but because disease activity is associated with changes in glycolytic enzyme expression in all major plaque cell types.

Plaque scRNA-seq data enable evaluation of alternative PET tracers of disease activity

The scRNA-seq and cellular proteome data from pigs with progressing or regressing atherosclerosis constitute a resource for evaluating other imaging markers of disease activity. To explore this potential, we analyzed the expression of the genes encoding the targets for several tracers that have been used to image atherosclerosis (*5*). Both

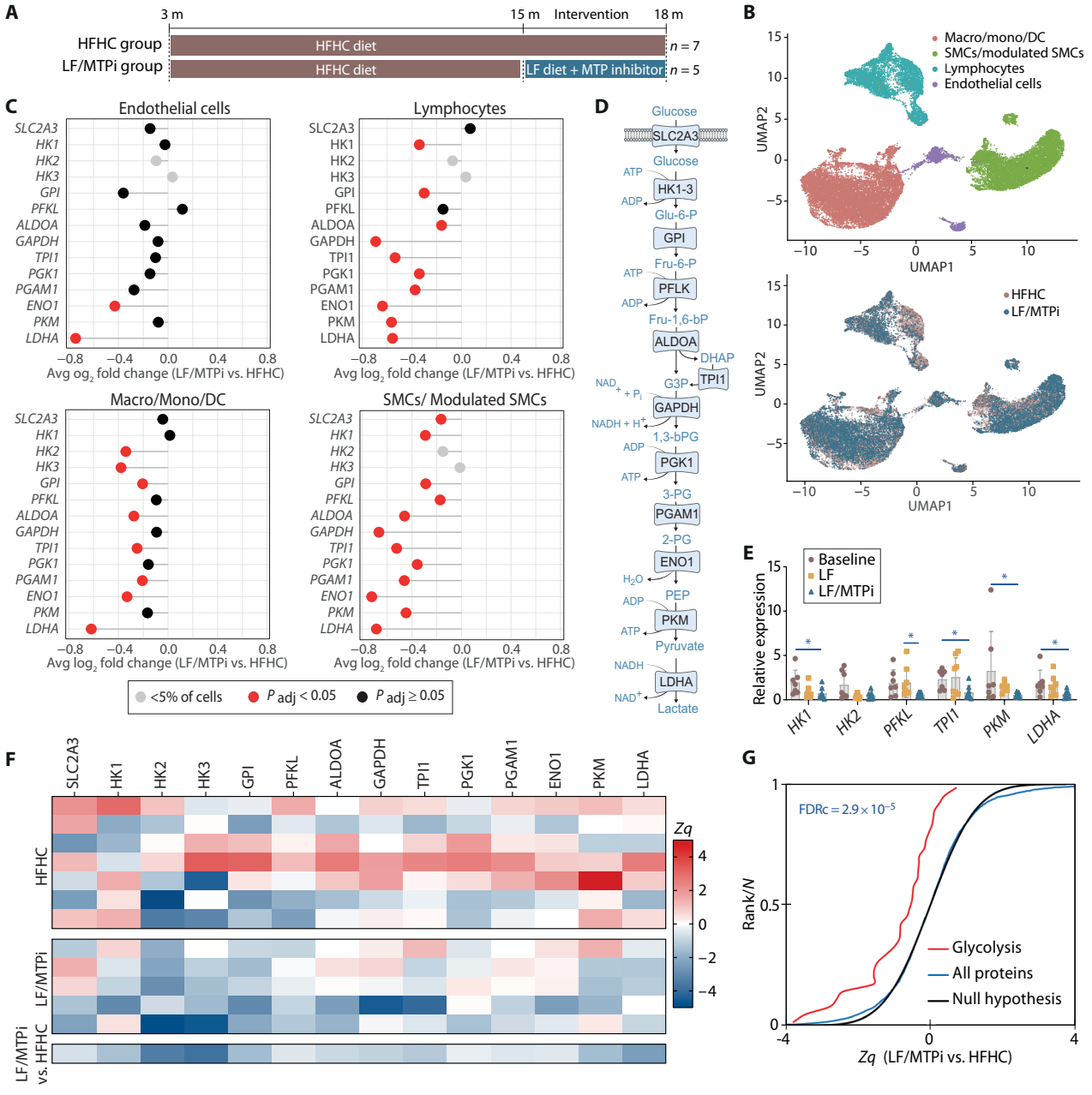

Fig. 7. Plaque glycolytic gene and protein expression are reduced upon APOB-LP lowering. (**A**) The experimental design timeline is shown to determine gene and protein expression signatures of abdominal plaque cells in progressing and regressing atherosclerosis. (**B**) Uniform manifold approximation and projection (UMAP) visualization of abdominal plaque scRNA-seq data from HFHC ($n = 6$) and LF/MTPi ($n = 5$) pigs. The top panel shows cell superclusters, including macrophages/monocytes/DCs, SMCs/modulated SMCs, lymphocytes, and endothelial cells. The bottom panel displays the contribution of each experimental group (HFHC or LF/MTPi) to clusters. (**C**) Plots showing differences in the expression of core glycolysis genes in LF/MTPi versus HFHC plaque cells in each supercluster. Significantly regulated genes (FDR-adjusted P value < 0.05) are shown in red. Genes detected in fewer than 5% of cells in either group (shown in light gray) were not considered. (**D**) Glycolysis pathway overview, illustrating the roles of the proteins encoded by the significantly regulated genes. (**E**) Quantitative RT-PCR analysis of abdominal aorta plaque samples from pigs in the ^{18}FDG-PET imaging experiment. Bars show means ± SEM. Statistical analysis for differences between baseline ($n = 7$), LF ($n = 8$), and LF/MTPi pigs ($n = 8$) was performed using one-way ANOVA with Tukey's posttest. *$P < 0.05$. (**F**) Heatmap of relative abundance changes (Zq values) of the glycolytic proteins encoded by the genes in (C) in HFHC ($n = 7$) and LF/MTPi ($n = 5$) pigs. (**G**) Analysis of coordinated abundance changes in glycolysis proteins using the SBT model (*50*). The plot shows the distribution of Zq values of glycolytic proteins (red line) compared with the total proteome (blue line). The statistical significance of the pathway change (FDRc) in comparison with the null hypothesis (black line) is indicated in the graph.

TSPO (*translocator protein*, encoding the target for ^{11}C-PK11195) and *VCAM1* (*vascular cell adhesion molecule 1*, encoding the target for ^{18}F-VAP-1) showed disease-linked regulation in at least one supercluster, although the effect was less robust than for glycolysis genes (Fig. 8). In contrast, the expression of *SSTR1* and *SSTR2* (*somatostatin receptor 1* and *somatostatin receptor 2*, encoding the target for ^{68}Ga-DOTATATE), was low, and no significant disease-linked regulation was detected for *FOLR2* (*folate receptor beta*, encoding the target for ^{18}F-FOL), *CXCR4* (*C-X-C motif chemokine receptor 4*, encoding the target for ^{68}Ga-Pentaxifor), and *ITGB3* and *ITGAV* (*integrin subunit beta 3* and *integrin subunit alpha V*, encoding the target for ^{18}F-Galacto-RGD) (Fig. 8). TSPO was not identified in the cellular proteome analysis (data file S2), which is not unexpected for a small transmembrane protein and should not detract from its promise as a target for imaging disease activity. No regulation of the other analyzed targets at the protein level was detected. Mining for alternative imaging targets can be performed in the scRNA-seq data and in the proteome data in data file S2.

DISCUSSION

In the present study, we demonstrate that ^{18}FDG-PET imaging can detect the decrease in disease activity induced by efficient APOB-LP lowering in *PCSK9*^{D374Y} minipigs. The reduction in APOB-LP–driven disease activity even reverted the signal to that of healthy aortas. The reduction in ^{18}FDG accumulation was not explained by changes in macrophage abundance, which was reduced only modestly after 3 months of APOB-LP lowering. Rather, the change was associated with the down-regulation of glycolytic gene expression in all major plaque cell types, including SMCs, macrophages, and lymphocytes, and by a reduced amount of glycolysis proteins in the plaque cellular proteome. These findings suggest that broad regulation of glycolysis across multiple cell types, rather than changes in inflammatory cell content, is the mechanism through which ^{18}FDG-PET imaging informs on disease activity in atherosclerosis.

The increased activation of glycolysis in progressing versus regressing atherosclerosis is consistent with the integral role of transcriptionally up-regulated aerobic glycolysis in the responses of macrophages, DCs, and T cells to damage-associated molecular patterns and antigens (*25*, *26*). Aerobic glycolysis provides macrophages and DCs with a rapid source of energy (*27*) and facilitates cholesterol and fatty-acid synthesis by promoting the generation of reducing equivalents through the pentose phosphate pathway, which is important for phagocytosis, endoplasmic reticulum expansion, and inflammasome activity (*26*, *28*, *29*). In helper and cytotoxic T lymphocytes, aerobic glycolysis also increases upon antigen binding (*27*). APOB-LPs drive atherosclerosis by acquiring molecular patterns that bind pattern-recognition and T cell receptors (*30*, *31*). It is, therefore, plausible that the reduction in modified APOB-LP in plaques after the LF/MTPi intervention induced the metabolic changes in immune cells. The metabolism of SMCs during phenotypic modulation and proliferation is less well studied, but platelet-derived growth factor–stimulated SMC proliferation involves up-regulated aerobic glycolysis in vitro (*32*, *33*), and experimentally forcing SMC glucose uptake accelerates atherosclerosis in mice (*34*).

The other main output of the present study is the *PCSK9*^{D374Y} minipig atherosclerosis regression model. In referring to the observed changes as plaque regression, we adopt the definition provided by Stary (*35*), who described regression as "any change in an established lesion that is favorable because it improves the course of the disease" and not necessarily a reduction in size or reversal to an earlier type of lesion. Compared with existing methods in mice, the *PCSK9*^{D374Y} pig features atherosclerotic lesions that are closer to human pathology in terms of size and plaque components. Compared with previous regression models in nonhuman primates and pigs, it provides much faster changes in plasma APOB-LP cholesterol; indeed, the LF/MTPi pigs exhibited a >75% drop in Apo-LP cholesterol within a week and reached clinical target concentrations for APOB-LP cholesterol in moderate- to high-risk patients within a month. Previous studies of plaque regression in large animals

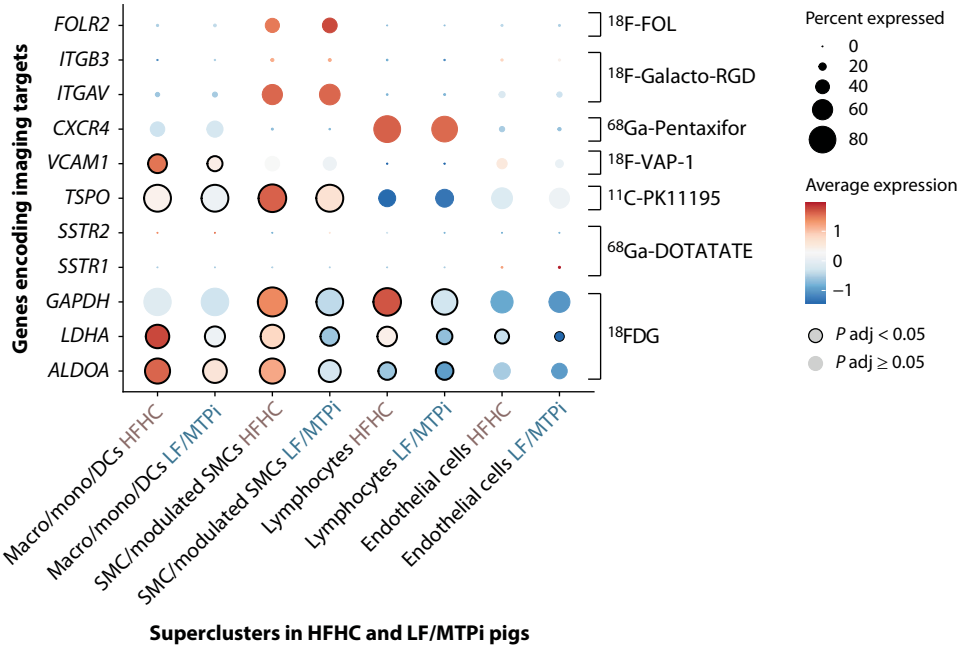

Fig. 8. scRNA-seq analysis of alternative PET tracer targets. Dot plot analysis shows the scaled expression of genes encoding targets for alternative PET tracers in scRNA-seq data from HFHC and LF/MTPi pigs. The genes encode the following markers: folate receptor β, targeted by ^{18}F-FOL; integrin αvβ3, targeted by ^{18}F-galacto-RGD; C-X-C motif chemokine receptor type 4, targeted by ^{68}Ga-Pentaxifor; vascular cell adhesion protein 1, targeted by ^{18}F-VAP-1; TSPO targeted by ^{11}C-PK111-95; and somatostatin receptors 1 and 2, targeted by ^{68}Ga-DOTATATE. *GAPDH*, *LDHA*, and *ALDOA* encode the glycolysis proteins glyceraldehyde 3-phosphate dehydrogenase, L-lactate dehydrogenase A chain, and aldolase A, indirectly targeted by ^{18}FDG. Data are provided for HFHC ($n = 6$) and LF/MTPi ($n = 5$) pigs in each supercluster. Dot size indicates expression prevalence, and color indicates the mean scaled expression amount. Significant differences in expression (FDR-adjusted P value < 0.05) between HFHC and LF/MTPi pigs are indicated with a black perimeter.

provided important insight into which plaque components can be regressed, but, based solely on dietary changes, they required long intervention times (*36*–*38*) and were thus less useful for investigating the plaque changes that account for the rapid reduction in coronary events in patients upon efficient APOB-LP lowering. It should be noted that the change from high- to low-fat diet in the *PCSK9* transgenic minipigs was not accompanied by a reduction in weight or plasma glucose, which is likely because the minipigs remain lean on the restricted high-fat feeding regimen.

The observed changes in regressing plaques of *PCSK9*^{D374Y} transgenic pigs are consistent with several key aspects of human plaque regression revealed in imaging studies. These include lipid depletion, detected by intravascular near-infrared spectroscopy (*39*); necrotic core shrinkage, recently demonstrated by CT angiography (*3*); and only minor changes in overall plaque size (*3*, *4*). It should be noted, however, that the pig model did not show fibrous cap thickening, in contrast with what has been reported in optical coherence tomography studies of patients undergoing APOB-LP–lowering therapy (*17*).

Plaque regression in the pig model is characterized by more persistent plaque inflammation than that observed in mouse models of atherosclerosis regression. In mouse models, global macrophage numbers are substantially reduced after only 4 weeks and are negligible after 3 months of APOB-LP lowering (*19*, *20*). Only the plaque shoulder showed a distinct reduction in inflammation within a similar time frame in the pig model. Plaque inflammation cannot be directly measured in humans in vivo, but the protective effect of anti-inflammatory medication on top of statin therapy in clinical trials suggests that plaque inflammation in humans is also less easily resolved (*40*). Thus, in addition to offering a test bed for imaging disease activity, the *PCSK9*^{D374Y} minipig atherosclerosis regression model could be used to test anti-inflammatory and other regression-promoting treatments for atherosclerosis.

The finding that plaque regression was followed by an increase in the number of mature SMC-supported vessel profiles was unexpected. Neovessels in human lesions have been linked to plaque inflammation, hemorrhage, and instability (*16*); how they respond to lipid lowering has not been studied, however. Although an increase in neovascularization during plaque regression may seem counterintuitive, other types of inflammatory resolution, such as in myocardial infarction or wound healing, are accompanied by transiently increased numbers of stabilized neovessels (*41*, *42*). Studies with longer regression periods are needed to understand whether the intraplaque vessels will eventually regress as disease activity in plaques is further reduced.

Our study has several limitations. First, we estimated glycolysis in individual cell types by the expression of glycolytic enzymes rather than by directly measuring cellular glycolytic fluxes, which would be technically challenging. Second, although we did not observe *MTP* expression in plaque cells or signs of MTPi-induced liver toxicity, it is difficult to rule out potential non–APOB-LP–mediated effects on atherosclerosis. Third, several experiments had a low number of replicates, and it is possible that more statistical power would reveal changes not detected in this study. Last, further studies are needed to validate the proposed mechanism in human atherosclerosis. It will also be of interest to examine the impact of other atherosclerosis-promoting factors and antiatherosclerotic therapies to determine whether changes in atherosclerotic disease activity are always associated with changes in glycolysis and, therefore, monitorable by ^{18}FDG-PET imaging.

Overall, this study provides insight into how ^{18}FDG-PET imaging can monitor plaque regression after ApoB-LP lowering in a large-animal model. By showing that multiple plaque cells, beyond immune cells, contribute to changes in ^{18}FDG-PET signal, the findings may guide the appropriate use of ^{18}FDG-PET as a clinical end point and enhance the interpretation of prior studies using this modality.

MATERIALS AND METHODS

Study design

The goal of this study was to describe changes in atherosclerotic plaque composition resulting from a 3-month APOB-LP–lowering intervention in *PCSK9*^{D374Y} transgenic minipigs and to determine whether the change in disease activity can be noninvasively monitored using ^{18}FDG-PET imaging. Two independent experiments were conducted. The first experiment (baseline = 7, LF = 8, and LF/MTPi = 8) was designed to assess changes in plaque composition and ^{18}FDG-PET signal. The second experiment (HFHC = 7 and LF/MTPi = 5) was conducted to analyze transcriptomic and proteomic changes in atherosclerotic plaques. In both experiments, atherosclerosis was induced by 12 months of an HFHC diet before animals were randomly assigned to experimental groups. Investigators performing data analysis were blinded to group identity. The first experiment used only male pigs to limit variability and was powered to detect a difference in SUV_{mean} of 15% at significance of $P < 0.05$ and with 90% statistical power, using data from a pilot experiment. The second experiment used $n = 5$ or 6 mixed-sex groups, which were considered sufficient for reproducible scRNA-seq and proteomics analysis. All replicates were biological replicates. No data were excluded, but some data points were not collected because of technical failures as detailed in table S1.

Animal procedures were reviewed by the ethical review boards at the Centro Nacional de Investigaciones Cardiovasculares (CNIC) and Universidad Autónoma de Madrid and approved by the Comunidad de Madrid (license nos. PROEX265/16 and 043.6/21).

BMS-212122 dose-calibration experiment

BMS-212122 is a chemical inhibitor of MTP with the IUPAC name 9-{4-[2,5-dimethyl-4-({[4′-(trifluoromethyl)-2-biphenylyl] carbonyl} amino)-1*H*-benzimidazol-1-*yl*]butyl}-*N*-(2,2,2-trifluoroethyl)-9*H*-fluorene-9-carboxamide. The inhibitor blocks the MTP-catalyzed transfer of triglycerides and cholesteryl esters to nascent APOB in the endoplasmic reticulum of hepatocytes and enterocytes, which is essential for assembling APOB-LPs, and thereby efficiently lowers plasma APOB-LP concentrations (*43*).

To confirm efficacy and decide on dosing, a dose-calibration study [1, 0.7, and 0.4 mg/(kg·day)] was performed in 10-month-old male *PCSK9*^{D374Y} minipigs maintained on standard pig feed ($n = 5$). BMS-212122 was dissolved in a small quantity of olive oil and mixed with feed. Treated minipigs ($n = 3$) received the dose mixed with the first food intake of the day, and other pigs ($n = 2$) served as negative controls. Each dose was administered for 1 week, followed by 1 week of washout.

^{18}FDG imaging experiments

Atherosclerosis was induced in 23 male *PCSK9*^{D374Y} transgenic minipigs by feeding them standard pig feed supplemented with 20% w/w lard, 1.5% w/w cholesterol, and 0.7% w/w NaCl (HFHC), from 3 until 15 months of age. During the first 6 months, the diet was also supplemented with 0.7% cholic acid. Animals were then either

euthanized (baseline group, $n = 7$), continued for 3 months on the standard (LF) pig feed (LF group, $n = 8$), or continued for 3 months on standard pig feed supplemented with BMS-212122 (LF/MTPi group, $n = 8$). The BMS-212122 dose was 1 mg/(kg·day) during the first week and 0.5 mg/(kg·day) for the rest of the intervention period. Blood samples were obtained from neck veins in the fasting state every 2 months during atherosclerosis induction, every month during the regression intervention, and for LF/MTPi pigs 1 week after initiating MTPi treatment. For nonatherosclerotic controls, we used age-matched nonatherosclerotic wild-type minipigs (healthy group, $n = 5$) maintained on standard pig feed from 3 to 15 months of age. Plasma measurements are described in the Supplementary Materials.

All minipigs underwent ^{18}FDG-PET imaging at the end of the study. Animals were fasted overnight and sedated with an intramuscular injection of azaperone (5 mg/kg), tiletamine and zolazepam (6 mg/kg), and medetomidine (0.1 mg/kg). After tracheal intubation, general anesthesia was maintained with vaporized isoflurane (1.5 to 1.8%). A surgical urinary catheter was placed to empty the bladder during scans, but bladder emptying was not always successful (precluding analysis of the iliac arteries). PET/CT images were acquired using a Gemini TF-64 scanner (Philips Healthcare) with the animals in the supine position. Each imaging sequence consisted of low-dose CT (120 kV and 200 mA) followed by PET acquisition 3 hours after the intravenous injection of 372 ± 81 MBq ^{18}FDG (Curium Pharma). PET scans were obtained across 10 bed positions with 50% bed overlap (3 min per bed) to ensure uniform sensitivity across the region of interest. Images were analyzed as detailed in Supplementary Materials and Methods.

Animals were euthanized 1 day after the PET scan. After sedation, animals were heparinized (300 units/kg, Braun) and then euthanized by intravenous injection of pentobarbital (50 mg/kg, Vetoquinol).

Histology and image analysis

Arteries were fixed in 4% buffered paraformaldehyde and embedded in paraffin or frozen in optimal cutting temperature (OCT) compound. Depending on the size of the pig, the paraffin-embedded tissue comprised 12 to 20 serial slices (each 4 mm) from the abdominal aorta (from the distal renal artery to the aortic trifurcation), 8 to 18 serial slices (each 4 mm) from the right common iliac artery, 8 to 10 serial slices (each 2 mm) from the proximal left anterior descending (LAD) coronary artery, and a single slice from the bifurcation of the LAD and CX coronary arteries (LAD-CX bifurcation) per pig. The OCT-embedded frozen tissue comprised 8 to 10 serial slices (each 2 mm) of the CX coronary artery, 8 to 18 slices (each 4 mm) of the left common iliac artery, and a single slice of the abdominal aorta (just above the proximal renal artery) per pig.

Sections were stained and imaged as detailed in the Supplementary Materials. Images were analyzed with Qupath 0.1.2 (*44*) and/or Fiji (Just ImageJ) using semiautomatic analysis (*45*). Analysis of neovessels was performed by manual counting of vessel profiles in anti-CD31–stained sections from the abdominal aorta. To increase certainty in the identification of CD31$^+$ or ACTA2$^+$ vessel profiles, only those with at least one erythrocyte in the lumen were considered. The study analyzed ~6500 images in total.

Plaque cell isolation from progressing and regressing atherosclerosis

To analyze gene and protein expression in progressing and regressing atherosclerosis, a separate set of *PCSK9*^{D374Y} minipigs ($n = 11$) was fed the same HFHC diet as above from ages 3 to 15 months to induce atherosclerosis. Minipigs were then randomized to remain on this diet (HFHC group, $n = 7$) or be changed to standard pig feed supplemented with BMS-212122 (LF/MTPi group, $n = 5$) for 3 months, with the same dosing as described above.

Animals were euthanized as described above, and the abdominal aorta was quickly isolated and opened. Atherosclerotic plaque tissue was dissected from the distal part of the abdominal aorta. The media, adventitia, and perivascular tissue were manually removed, and ~200 to 250 mg of plaque tissue was washed in Hanks' balanced salt solution and minced. The tissue was incubated for 60 min at 37°C in 1 ml of enzyme solution containing elastase [1.5 mg/ml (8 U/ml); LS002279, Worthington Biochemical], liberase (2 mg/ml; 05401119001, Sigma-Aldrich), and deoxyribonuclease I (300 μg/ml; Sigma-Aldrich, DN25). Nondigested tissue was disaggregated using a smooth-tipped Pasteur pipette. Reactions were stopped by adding phosphate-buffered saline containing 0.5% bovine serum albumin (PBS and 0.5% BSA). The suspension was passed through a 70-μm pore filter to remove aggregates, and cells were collected by centrifugation and resuspended in 500 μl of PBS and 0.5% BSA. 4′,6-Diamidino-2-phenylindole (DAPI; final concentration, 1 μg/ml) and Draq5 (Thermo Fisher Scientific, 65-0880-96; final concentration, 5 μM) were added, and viable cells (Draq5 positive and DAPI negative) were sorted in a FACSAria Cell Sorter.

scRNA-seq analysis

The viability and counts of sorted cells were checked with a Countess III cell counter (Thermo Fisher Scientific), and 10,000 to 16,500 cells from HFHC ($n = 6$) and LF/MTPi ($n = 5$) pigs were loaded into each port of a Chromium Next GEM Chip G (10x Genomics). After reverse transcription (RT) and cDNA amplification, sequencing libraries were prepared using the Chromium Next GEM Single Cell 3' Kit v3.1 (10x Genomics). Mean library size was calculated using a 2100 Bioanalyzer (Agilent), and the concentration was determined with a Qubit fluorometer (Thermo Fisher Scientific). Libraries were sequenced in paired-end reads using a HiSeq 4000 system (Illumina) and processed with RTA v1.18.66.3. FASTQ files for each sample were obtained using the CellRanger demux pipeline (10x Genomics).

FASTQ files for the 11 independent samples were processed using 10X CellRanger software (v6.0.0) with *Sus scrofa* genome reference Ss11.1 (Ensembl gene build v109). Pseudogenes and small RNAs were removed from the reference. Gene metadata were obtained from the corresponding Ensembl BioMart archive. Filtration of barcodes [1000 < UMIs (unique molecular identifiers) < 30,000, detected genes > 600, percentage of mitochondrial reads < 15%, percentage of ribosomal genes < 30%, percentage of hemoglobin reads < 0.1%, cell UMIs/total > 0.2%, < 50% of reads from top 50 expressed genes], clustering, and expression analysis were performed using Seurat and scatter R packages running in R version 4.1.2. For rigorous doublet identification, two approaches were combined: DoubletFinder version 2.0.4 (*46*) and scDblFinder version 1.12.0 (*47*) with an assumed doublet rate of 15%. Only cells that were singlets by both methods were retained in the analysis. A total of 26,807 cells were retained for the final analysis (2560.5 and 2683 median number of cells per pig in the HFHC and LF/MTPi groups, respectively). Count matrices were merged, log normalized, and scaled. Mitochondrial and hemoglobin genes were removed. Highly variable features (2000) were selected using the vst algorithm. For the principal components analysis, the

first 30 components were used. After clustering (resolution 0.2), 10 clusters were identified and annotated on the basis of cell markers from the literature, and clusters were merged on the basis of belonging to four main cell types: macros/monos/DCs, SMCs/modulated SMCs, lymphocytes, and endothelial cells. Differential expression analysis between the LF/MTPi and HFHC groups was performed in each supercluster using the MAST method (*min.pct* = 0.05). Differences in the expression of metabolic pathway genes (WP534, glycolysis; WP78, tricarboxylic acid (TCA) cycle; WP111, OXPHOS system; WP134, pentose phosphate metabolism; WP143, fatty-acid β-oxidation; and WP3925, amino acid metabolism from WikiPathways) between groups were plotted using ggplot2 v3.4.2. Expression of key genes was validated in plaque sections by quantitative RT-PCR using primers in table S2 as described in the Supplementary Materials.

Proteomics

Frozen residual viable sorted cells (130,000 to 400,000 cells per animal) from all HFHC ($n = 7$) and LF/MTPi ($n = 5$) pigs were resuspended with 70 μl of a buffer containing 50 mM tris, 2% SDS, and 10 mM dithiothreitol and boiled for 5 min for protein denaturation. Extracted proteins (~100 μg) were subjected to in-filter reduction and alkylation using iodoacetamide followed by trypsin digestion (Nanosep Centrifugal Devices with Omega Membrane-10 K, PALL), as described (*48*). Each sample was subjected to liquid chromatography–tandem mass spectrometry (MS) analysis using an EV1113 Endurance column (Evosep) heated to 50° and interfaced with the Thermo Orbitrap Eclipse Mass Spectrometer (Thermo Fisher Scientific) using an EASY-Spray Ion Source. Samples were separated on an Evosep One LC system using the preprogrammed gradient for 15 samples per day. Data were collected using data-independent acquisition. Full MS resolution was set to 120,000 at a mass/charge ratio (m/z) of 200, and the full MS automatic gain control (AGC) target was 300% with a maximum injection time (IT) of 246 ms. The AGC target value for fragment spectra was set to 1000%. Fifty windows of 12 Th scanning from 400 to 1000 m/z were used with an overlap of 1 Da. MS2 resolution was set to 30,000, IT to 54 ms, and normalized collision energy to 30%. Raw files were analyzed with DIA-NN (1.8.1) (*49*) using an in silico predicted library from the *Sus scrofa* proteome (UniProt database, July 2023 release) containing cRAP (common Repository of Adventitious Proteins). For library prediction, precursor mass range was set from 400 to 1000, allowing one missed cleavage, N-terminal Met excision, variable oxidation in Met, and fixed Cys carbamidomethylation. A 1% false discovery rate (FDR) was used as the criterion for peptide identification.

The quantitative information was integrated to the protein level using the Generic Integration Algorithm (*50*) with iSanXoT (*51*, *52*), using the preprogramed label-free quantification workflow. Quantitative protein values were expressed as relative abundances in relation to the average of control (HFHC) samples using the standardized variable Zq (normalized $\log_2$ ratios expressed in units of SD according to the estimated variances). For systems biology analysis, we applied the Systems Biology Triangle (SBT) algorithm (*50*), which detects statistically significant abundance changes in functional categories produced by the coordinated behavior of proteins, in iSanXoT using the preprogrammed SBT workflow. Proteins were functionally annotated using the Gene Ontology database (June 2023), which was manually curated for the glycolysis pathway to include the proteins encoded by the WP534 gene set used for scRNA-seq analysis.

Statistical analysis

Linear regression analyses were performed after confirming normal distribution of residuals and homoscedasticity. For multiple-group comparisons, normally distributed data were analyzed by analysis of variance (ANOVA) with Tukey's posttest or, in cases with unequal variance, by Brown-Forsythe and Welch ANOVA with Dunnett's T3 posttest, whereas nonnormally distributed data were analyzed with the Kruskal-Wallis test with Dunn's posttest. Multiple unpaired t tests with adjustment of significance by the Holm-Šidák method were used for repeated two-group comparisons. Analyses were conducted using Prism (GraphPad Software Inc.) and Excel (Microsoft). All tests were two tailed, and statistical significance was assigned at $P < 0.05$.

Supplementary Materials

The PDF file includes:
Materials and Methods
Figs. S1 to S11
Tables S1 and S2
Legends for data files S1 and S2

Other Supplementary Material for this manuscript includes the following:
Data files S1 and S2
MDAR Reproducibility Checklist

REFERENCES AND NOTES

1. U. Baber, R. Mehran, S. Sartori, M. M. Schoos, H. Sillesen, P. Muntendam, M. J. Garcia, J. Gregson, S. Pocock, E. Falk, V. Fuster, Prevalence, impact, and predictive value of detecting subclinical coronary and carotid atherosclerosis in asymptomatic adults: The BioImage study. *J. Am. Coll. Cardiol.* **65**, 1065–1074 (2015).
2. L. Räber, Y. Ueki, T. Otsuka, S. Losdat, J. D. Häner, J. Lonborg, G. Fahrni, J. F. Iglesias, R.-J. van Geuns, A. S. Ondracek, M. D. Radu Juul Jensen, C. Zanchin, S. Stortecky, D. Spirk, G. C. M. Siontis, L. Saleh, C. M. Matter, J. Daemen, F. Mach, D. Heg, S. Windecker, T. Engstrøm, I. M. Lang, K. C. Koskinas, PACMAN-AMI collaborators, Effect of alirocumab added to high-intensity statin therapy on coronary atherosclerosis in patients with acute myocardial infarction: The PACMAN-AMI randomized clinical trial. *JAMA* **327**, 1771–1781 (2022).
3. L. Pérez de Isla, J. L. Díaz-Díaz, M. J. Romero, O. Muñiz-Grijalvo, J. D. Mediavilla, R. Argüeso, R. de Andrés, F. Fuentes, J. F. Sánchez Muñoz-Torrero, P. Rubio, P. Álvarez-Baños, D. Mañas, L. Suárez Gutierrez, A. Saltijeral Cerezo, P. Mata, SAFEHEART Investigators, Characteristics of coronary atherosclerosis related to plaque burden regression during treatment with alirocumab: The ARCHITECT study. *Circ. Cardiovasc. Imaging* **17**, e016206 (2024).
4. L. P. Dawson, M. Lum, N. Nerleker, S. J. Nicholls, J. Layland, Coronary atherosclerotic plaque regression: JACC state-of-the-art review. *J. Am. Coll. Cardiol.* **79**, 66–82 (2022).
5. M. L. Senders, C. Calcagno, A. Tawakol, M. Nahrendorf, W. J. M. Mulder, Z. A. Fayad, PET/MR imaging of inflammation in atherosclerosis. *Nat. Biomed. Eng.* **7**, 202–220 (2023).
6. R. S. Sriranjan, J. M. Tarkin, N. R. Evans, E. P. V. Le, M. M. Chowdhury, J. H. F. Rudd, Atherosclerosis imaging using PET: Insights and applications. *Br. J. Pharmacol.* **178**, 2186–2203 (2021).
7. A. Tawakol, Z. A. Fayad, R. Mogg, A. Alon, M. T. Klimas, H. Dansky, S. S. Subramanian, A. Abdelbaky, J. H. F. Rudd, M. E. Farkouh, I. O. Nunes, C. R. Beals, S. S. Shankar, Intensification of statin therapy results in a rapid reduction in atherosclerotic inflammation: Results of a multicenter fluorodeoxyglucose-positron emission tomography/computed tomography feasibility study. *J. Am. Coll. Cardiol.* **62**, 909–917 (2013).
8. D. F. van Wijk, B. Sjouke, A. Figueroa, H. Emami, F. M. van der Valk, M. H. MacNabb, L. C. Hemphill, D. M. Schulte, M. G. Koopman, M. E. Lobatto, H. J. Verberne, Z. A. Fayad, J. J. P. Kastelein, W. J. M. Mulder, G. K. Hovingh, A. Tawakol, E. S. G. Stroes, Nonpharmacological lipoprotein apheresis reduces arterial inflammation in familial hypercholesterolemia. *J. Am. Coll. Cardiol.* **64**, 1418–1426 (2014).
9. R. M. Hoogeveen, T. S. J. Opstal, Y. Kaiser, L. C. A. Stiekema, J. Kroon, R. J. J. Knol, W. A. Bax, H. J. Verberne, J. H. Cornel, E. S. G. Stroes, PCSK9 antibody alirocumab attenuates arterial wall inflammation without changes in circulating inflammatory markers. *JACC Cardiovasc. Imaging* **12**, 2571–2573 (2019).
10. J. H. F. Rudd, E. A. Warburton, T. D. Fryer, H. A. Jones, J. C. Clark, N. Antoun, P. Johnström, A. P. Davenport, P. J. Kirkpatrick, B. N. Arch, J. D. Pickard, P. L. Weissberg, Imaging atherosclerotic plaque inflammation with [^{18}F]-fluorodeoxyglucose positron emission tomography. *Circulation* **105**, 2708–2711 (2002).

11. A. Tawakol, R. Q. Migrino, G. G. Bashian, S. Bedri, D. Vermylen, R. C. Cury, D. Yates, G. M. LaMuraglia, K. Furie, S. Houser, H. Gewirtz, J. E. Muller, T. J. Brady, A. J. Fischman, In vivo 18F-fluorodeoxyglucose positron emission tomography imaging provides a noninvasive measure of carotid plaque inflammation in patients. *J. Am. Coll. Cardiol.* **48**, 1818–1824 (2006).
12. R. H. Al-Mashhadi, L. P. Tolbod, L. Ø. Bloch, M. M. Bjørklund, Z. P. Nasr, Z. Al-Mashhadi, M. Winterdahl, J. Frøkiær, E. Falk, J. F. Bentzon, ^{18}Fluorodeoxyglucose accumulation in arterial tissues determined by PET signal analysis. *J. Am. Coll. Cardiol.* **74**, 1220–1232 (2019).
13. R. H. Al-Mashhadi, C. B. Sørensen, P. M. Kragh, C. Christoffersen, M. B. Mortensen, L. P. Tolbod, T. Thim, Y. Du, J. Li, Y. Liu, B. Moldt, M. Schmidt, G. Vajta, T. Larsen, S. Purup, L. Bolund, L. B. Nielsen, H. Callesen, E. Falk, J. G. Mikkelsen, J. F. Bentzon, Familial hypercholesterolemia and atherosclerosis in cloned minipigs created by DNA transposition of a human PCSK9 gain-of-function mutant. *Sci. Transl. Med.* **5**, 166ra1 (2013).
14. D. J. Blom, M. R. Averna, E. A. Meagher, H. du Toit Theron, C. R. Sirtori, R. A. Hegele, P. K. Shah, D. Gaudet, C. Stefanutti, G. B. Vigna, D. Larrey, L. T. Bloedon, P. Foulds, D. J. Rader, M. Cuchel, Long-term efficacy and safety of the microsomal triglyceride transfer protein inhibitor lomitapide in patients with homozygous familial hypercholesterolemia. *Circulation* **136**, 332–335 (2017).
15. F. Mach, C. Baigent, A. L. Catapano, K. C. Koskinas, M. Casula, L. Badimon, M. J. Chapman, G. G. De Backer, V. Delgado, B. A. Ference, I. M. Graham, A. Halliday, U. Landmesser, B. Mihaylova, T. R. Pedersen, G. Riccardi, D. J. Richter, M. S. Sabatine, M.-R. Taskinen, L. Tokgozoglu, O. Wiklund, ESC Scientific Document Group, 2019 ESC/EAS Guidelines for the management of dyslipidaemias: Lipid modification to reduce cardiovascular risk. *Eur. Heart J.* **41**, 111–188 (2020).
16. J. F. Bentzon, F. Otsuka, R. Virmani, E. Falk, Mechanisms of plaque formation and rupture. *Circ. Res.* **114**, 1852–1866 (2014).
17. H. Yano, S. Horinaka, T. Ishimitsu, Effect of evolocumab therapy on coronary fibrous cap thickness assessed by optical coherence tomography in patients with acute coronary syndrome. *J. Cardiol.* **75**, 289–295 (2020).
18. J. Shim, R. H. Al-Mashhadi, C. B. Sørensen, J. F. Bentzon, Large animal models of atherosclerosis–New tools for persistent problems in cardiovascular medicine. *J. Pathol.* **238**, 257–266 (2016).
19. L. Carramolino, J. Albarrán-Juárez, A. Markov, E. Hernández-SanMiguel, D. Sharysh, V. Cumbicus, D. Morales-Cano, V. Labrador-Cantarero, P. L. Møller, P. Nogales, A. Benguria, A. Dopazo, F. Sanchez-Cabo, C. Torroja, J. F. Bentzon, Cholesterol lowering depletes atherosclerotic lesions of smooth muscle cell-derived fibromyocytes and chondromyocytes. *Nat. Cardiovasc. Res.* **3**, 203–220 (2024).
20. M. Peled, H. Nishi, A. Weinstock, T. J. Barrett, F. Zhou, A. Quezada, E. A. Fisher, A wild-type mouse-based model for the regression of inflammation in atherosclerosis. *PLOS ONE* **12**, e0173975 (2017).
21. P. D. Richardson, M. J. Davies, G. V. Born, Influence of plaque configuration and stress distribution on fissuring of coronary atherosclerotic plaques. *Lancet* **2**, 941–944 (1989).
22. H.-S. Han, G. Kang, J. S. Kim, B. H. Choi, S.-H. Koo, Regulation of glucose metabolism from a liver-centric perspective. *Exp. Mol. Med.* **48**, e218 (2016).
23. H. Ngo, S. M. Tortorella, K. Ververis, T. C. Karagiannis, The Warburg effect: Molecular aspects and therapeutic possibilities. *Mol. Biol. Rep.* **42**, 825–834 (2015).
24. S.-C. Cheng, J. Quintin, R. A. Cramer, K. M. Shepardson, S. Saeed, V. Kumar, E. J. Giamarellos-Bourboulis, J. H. A. Martens, N. A. Rao, A. Aghajanirefah, G. R. Manjeri, Y. Li, D. C. Ifrim, R. J. W. Arts, B. M. J. W. van der Veer, P. M. T. Deen, C. Logie, L. A. O'Neill, P. Willems, F. L. van de Veerdonk, J. W. M. van der Meer, A. Ng, L. A. B. Joosten, C. Wijmenga, H. G. Stunnenberg, R. J. Xavier, M. G. Netea, mTOR- and HIF-1α-mediated aerobic glycolysis as metabolic basis for trained immunity. *Science* **345**, 1250684 (2014).
25. L. Almeida, A. Dhillon-LaBrooy, T. Sparwasser, The evolutionary tug-of-war of macrophage metabolism during bacterial infection. *Trends Endocrinol. Metab.* **35**, 235–248 (2024).
26. D. F. J. Ketelhuth, E. Lutgens, M. Bäck, C. J. Binder, J. Van den Bossche, C. Daniel, I. E. Dumitriu, I. Hoefer, P. Libby, L. O'Neill, C. Weber, P. C. Evans, Immunometabolism and atherosclerosis: Perspectives and clinical significance: A position paper from the Working Group on Atherosclerosis and Vascular Biology of the European Society of Cardiology. *Cardiovasc. Res.* **115**, 1385–1392 (2019).
27. N. M. Chapman, M. R. Boothby, H. Chi, Metabolic coordination of T cell quiescence and activation. *Nat. Rev. Immunol.* **20**, 55–70 (2020).
28. K. K. Y. Ting, J. Jongstra-Bilen, M. I. Cybulsky, The multi-faceted role of NADPH in regulating inflammation in activated myeloid cells. *Front. Immunol.* **14**, 1328484 (2023).
29. P. Cheng, R. C. Wirka, J. B. Kim, H.-J. Kim, T. Nguyen, R. Kundu, Q. Zhao, D. Sharma, A. Pedroza, M. Nagao, D. Iyer, M. P. Fischbein, T. Quertermous, Smad3 regulates smooth muscle cell fate and mediates adverse remodeling and calcification of the atherosclerotic plaque. *Nat. Cardiovasc. Res.* **1**, 322–333 (2022).
30. J. Borén, C. J. Packard, C. J. Binder, Apolipoprotein B-containing lipoproteins in atherogenesis. *Nat. Rev. Cardiol.* **22**, 399–413 (2025).
31. I. Raposo-Gutiérrez, A. Rodríguez-Ronchel, A. R. Ramiro, Atherosclerosis antigens as targets for immunotherapy. *Nat. Cardiovasc. Res.* **2**, 1129–1147 (2023).
32. J. Shi, Y. Yang, A. Cheng, G. Xu, F. He, Metabolism of vascular smooth muscle cells in vascular diseases. *Am. J. Physiol. Heart Circ. Physiol.* **319**, H613–H631 (2020).
33. M. Werle, J. Kreuzer, J. Höfele, A. Elsässer, C. Ackermann, H. A. Katus, A. M. Vogt, Metabolic control analysis of the Warburg-effect in proliferating vascular smooth muscle cells. *J. Biomed. Sci.* **12**, 827–834 (2005).
34. V. Z. Wall, S. Barnhart, J. E. Kanter, F. Kramer, M. Shimizu-Albergine, N. Adhikari, T. N. Wight, J. L. Hall, K. E. Bornfeldt, Smooth muscle glucose metabolism promotes monocyte recruitment and atherosclerosis in a mouse model of metabolic syndrome. *JCI Insight* **3**, e96544 (2018).
35. *An Atlas of Atherosclerosis Progression and Regression*, H. C. Stary, Ed. (CRC Press, ed. 1, 1999); www.taylorfrancis.com/books/9780203490709.
36. K. E. Fritz, J. M. Augustyn, J. Jarmolych, A. S. Daoud, K. T. Lee, Regression of advanced atherosclerosis in swine: Chemical studies. *Arch. Pathol. Lab. Med.* **100**, 380–385 (1976).
37. A. S. Daoud, J. Jarmolych, J. M. Augustyn, K. E. Fritz, Sequential morphologic studies of regression of advanced atherosclerosis. *Arch. Pathol. Lab. Med.* **105**, 233–239 (1981).
38. J. P. Strong, A. K. Bhattacharyya, D. A. Eggen, H. C. Stary, G. T. Malcom, W. P. Newman, C. Restrepo, Long-term induction and regression of diet-induced atherosclerotic lesions in rhesus monkeys. II. Morphometric evaluation of lesions by light microscopy in coronary and carotid arteries. *Arterioscler. Thromb.* **14**, 2007–2016 (1994).
39. A. S. Kini, U. Baber, J. C. Kovacic, A. Limaye, Z. A. Ali, J. Sweeny, A. Maehara, R. Mehran, G. Dangas, G. S. Mintz, V. Fuster, J. Narula, S. K. Sharma, P. R. Moreno, Changes in plaque lipid content after short-term intensive versus standard statin therapy: The YELLOW trial (reduction in yellow plaque by aggressive lipid-lowering therapy). *J. Am. Coll. Cardiol.* **62**, 21–29 (2013).
40. O. Soehnlein, P. Libby, Targeting inflammation in atherosclerosis - from experimental insights to the clinic. *Nat. Rev. Drug Discov.* **20**, 589–610 (2021).
41. N. Frangogiannis, The immune system and cardiac repair. *Pharmacol. Res.* **58**, 88–111 (2008).
42. J. A. Flegg, S. N. Menon, H. M. Byrne, D. L. S. McElwain, A current perspective on wound healing and tumour-induced angiogenesis. *Bull. Math. Biol.* **82**, 23 (2020).
43. J. A. Robl, R. Sulsky, C. Q. Sun, L. M. Simpkins, T. Wang, J. K. Dickson, Y. Chen, D. R. Magnin, P. Taunk, W. A. Slusarchyk, S. A. Biller, S. J. Lan, F. Connolly, L. K. Kunselman, T. Sabrah, H. Jamil, D. Gordon, T. W. Harrity, J. R. Wetterau, A novel series of highly potent benzimidazole-based microsomal triglyceride transfer protein inhibitors. *J. Med. Chem.* **44**, 851–856 (2001).
44. P. Bankhead, M. B. Loughrey, J. A. Fernández, Y. Dombrowski, D. G. McArt, P. D. Dunne, S. McQuaid, R. T. Gray, L. J. Murray, H. G. Coleman, J. A. James, M. Salto-Tellez, P. W. Hamilton, QuPath: Open source software for digital pathology image analysis. *Sci. Rep.* **7**, 16878 (2017).
45. J. Schindelin, I. Arganda-Carreras, E. Frise, V. Kaynig, M. Longair, T. Pietzsch, S. Preibisch, C. Rueden, S. Saalfeld, B. Schmid, J.-Y. Tinevez, D. J. White, V. Hartenstein, K. Eliceiri, P. Tomancak, A. Cardona, Fiji: An open-source platform for biological-image analysis. *Nat. Methods* **9**, 676–682 (2012).
46. C. S. McGinnis, L. M. Murrow, Z. J. Gartner, DoubletFinder: Doublet detection in single-cell RNA sequencing data using artificial nearest neighbors. *Cell Syst.* **8**, 329–337.e4 (2019).
47. P.-L. Germain, A. Lun, C. Garcia Meixide, W. Macnair, M. D. Robinson, Doublet identification in single-cell sequencing data using scDblFinder. *F1000Res* **10**, 979 (2021).
48. J. R. Wiśniewski, A. Zougman, N. Nagaraj, M. Mann, Universal sample preparation method for proteome analysis. *Nat. Methods* **6**, 359–362 (2009).
49. V. Demichev, C. B. Messner, S. I. Vernardis, K. S. Lilley, M. Ralser, DIA-NN: Neural networks and interference correction enable deep proteome coverage in high throughput. *Nat. Methods* **17**, 41–44 (2020).
50. F. García-Marqués, M. Trevisan-Herraz, S. Martínez-Martínez, E. Camafeita, I. Jorge, J. A. Lopez, N. Méndez-Barbero, S. Méndez-Ferrer, M. A. Del Pozo, B. Ibáñez, V. Andrés, F. Sánchez-Madrid, J. M. Redondo, E. Bonzon-Kulichenko, J. Vázquez, A novel systems-biology algorithm for the analysis of coordinated protein responses using quantitative proteomics. *Mol. Cell. Proteomics* **15**, 1740–1760 (2016).
51. M. Trevisan-Herraz, N. Bagwan, F. García-Marqués, J. M. Rodriguez, I. Jorge, I. Ezkurdia, E. Bonzon-Kulichenko, J. Vázquez Eds, SanXoT: A modular and versatile package for the quantitative analysis of high-throughput proteomics experiments. *Bioinformatics* **35**, 1594–1596 (2019).
52. J. M. Rodríguez, I. Jorge, A. Martinez-Val, R. Barrero-Rodríguez, R. Magni, E. Núñez, A. Laguillo, C. A. Devesa, J. A. López, E. Camafeita, J. Vázquez, iSanXoT: A standalone application for the integrative analysis of mass spectrometry-based quantitative proteomics data. *Comput. Struct. Biotechnol. J.* **23**, 452–459 (2024).
53. Y. Perez-Riverol, C. Bandla, D. J. Kundu, S. Kamatchinathan, J. Bai, S. Hewapathirana, N. S. John, A. Prakash, M. Walzer, S. Wang, J. A. Vizcaíno, The PRIDE database at 20 years: 2025 Update. *Nucleic Acids Res.* **53**, D543–D553 (2025).

Acknowledgments: We thank members of the CNIC Animal Facility and Histopathology Unit, Microscopy Unit, Genomics Unit, Bioinformatics Unit, and Cellomics Unit for excellent technical help and S. Bartlett, CNIC, for English editing. We also extend our thanks to Bristol Myers Squibb for providing BMS-212122 and D. Gordon, Bristol Myers Squibb, for helpful advice on dosing. **Funding:** This work was supported by the European Research Council (ERC) under the European Union's Horizon 2020 research and innovation programme (grant agreement no. 866240 to J.F.B.); Ministerio de Economía, Industria y Competitividad (MEIC) with cofunding from the European Regional Development Fund (ERDF) (grants PI2019-108568RB-I00 to J.F.B., BES-2016-076633 to P.N., and PID2021-122348NB-I00 to J.V.); Instituto de Salud Carlos III with cofunding from ERDF/European "A way to make Europe" (grant PI20/00610 to J.M.); the Comunidad de Madrid (grant S2022/BMD-7333-CM to J.V.); and Fundación Obra Social La Caixa (AtheroConvergence, HR20-00075 to J.F.B., and LCF/PR/HR22/52420019 to J.V.). The Centro Nacional de Investigaciones Cardiovasculares (CNIC) is supported by the Instituto de Salud Carlos III (ISCIII), the Ministerio de Ciencia e Innovación (MICIN), and the Pro CNIC Foundation and is a Severo Ochoa Center of Excellence (grant CEX2020001041-S funded by MICIN/AEI/10.13039/501100011033). **Author contributions:** P.N. and J.F.B. conceptualized the study; planned experiments, methodology, and analysis; and wrote the manuscript with input from all authors. P.N., J.V., J.M., and J.F.B. acquired funding. P.N. and L.G.-C. acquired and analyzed plasma and histology samples. P.N., C.V., A.M.-C., R.A.M., S.E., and J.M. performed the 18FDG-PET/CT experiments, and P.N., C.V., A.M.-C., S.E., and J.M. analyzed scans. P.N., D.M.-C., and L.C. isolated plaque cells for scRNA-seq, which was performed by A.B. and A.D. and analyzed by D.S., C.T., R.I.-S., and F.S.-C. D.d.R.-A. carried out proteomics analysis, which was analyzed by D.d.R.-A. and J.V. Data curation was performed by P.N., C.T., and D.d.R.-A. **Competing interests:** J.F.B. has provided consulting to and received research grants from Novo Nordisk A/S. The PCSK9 transgenic minipig line is covered by US Patent 8546643 (pig model for atherosclerosis). All other authors declare that they have no competing interests. **Data and materials availability:** All data associated with this study are present in the paper or the Supplementary Materials. scRNA-seq data have been deposited in BioStudies (ArrayExpress) with accession no. E-MTAB-13898 as well as on the European Nucleotide Archive with accession number ERP158494. The deposited scRNA-data can also be explored interactively through the Single Cell Data Visualization platform (scDAVIS) at https://bioinfo.cnic.es/scdavis/. The mass spectrometry proteomics data have been deposited to the ProteomeXchange Consortium through the PRIDE (*53*) partner repository with the dataset identifier PXD060147. The code used for the scRNA-seq analysis is available at https://zenodo.org/records/15801369. BMS-212122 was provided by Bristol Myers Squibb under a material transfer agreement but is also commercially available. The transgenic minipigs can be made available under a material transfer agreement with Aarhus University.

Submitted 13 March 2024
Resubmitted 3 March 2025
Accepted 16 July 2025
Published 13 August 2025
10.1126/scitranslmed.ado6467